LUNDS UNIVERSITET

Measuring longitudinal bunch profiles using Time-Correlated Single-Photon Counting at MAX IV Laboratory

---

A thesis presented for the degree of

Bachelor of Physics

by

Johann Schmand

Project duration: 2 months

Supervisor: Francesca Curbis

Co-supervisor: Miriam Brosi

Department of Physics,

Division of Synchrotron Radiation Research

Date of examination: June 4, 2024

Abstract

MAX IV laboratory is a modern synchrotron light source, providing synchrotron radiation for a wide array of research groups. To provide users with high-quality synchrotron radiation, the electron beam from which the synchrotron radiation stems needs to be well understood. This thesis describes a first implementation of time-correlated single-photon counting (TCSPC) as a tool to measure longitudinal bunch profiles of the electron beam. An overview of the measurement system is given, and the data analysis process is discussed. In this thesis, the focus of data analysis was to compensate for timing jitter caused by the various components in the measurement system.

TCSPC, in theory, offers significant advantages over established methods to measure longitudinal bunch profiles at MAX IV, namely that it allows for measurements of all bunches' profiles in a storage ring simultaneously, without light from different bunches interfering. To implement TCSPC as a measurement tool at MAX IV, a number of steps were taken. The photon detector timing jitter (or transit time spread, TTS) in dependence of wavelength of incoming synchrotron light was determined. For further measurements, a bandpass filter was used with the detectors to minimize their TTSs. Furthermore, the detector TTSs were characterized using measurements involving short laser pulses. The most important measurements within this work, however, were measurements taken to determine the TTS of the measurement system as a whole. This was done by use of a known bunch profile, which allows the extraction of the system TTS from raw data. Once determined, the system TTSs were used as a correction to measurements of electron beams under different conditions, to test the viability of the TCSPC setup.

The overall conclusion is that a first approach to TCSPC has been successfully implemented at MAX IV. Compared to conventional measurement techniques of longitudinal bunch profiles, such as using a streak camera, TCSPC measurements offer the advantage that light from adjacent bunches does not overlap, meaning that bunch profiles can be studied individually. Furthermore, the intra-bunch resolution is superior to that of the streak camera, and TCSPC measurements are significantly less noisy than streak camera measurements. The implementation of TCSPC as it stands has a number of limitations, however, mainly that it is not entirely clear whether the determined system TTSs are fully independent of measured bunch profiles.

Table of contents

Acknowledgements

List of acronyms and abbreviations

FWHM   Full width at half maximum

IR   Infra-red

MO   Master oscillator

ND   Neutral density (used in the context of optical filters)

PMA   Photomultiplier detector assembly (a single-photon detector, effectively a photomultiplier tube)

RF   Radio frequency

RMS   Root mean square

SPAD   Single-photon avalanche diode (a type of single-photon detector)

TCSPC   Time-correlated single-photon counting

TTS   Transit time spread (timing jitter)

1 Introduction

Since its discovery, synchrotron radiation has proven tremendously useful in the study of material structure and properties. At modern synchrotron light sources, many different research groups each working on their own experiments are present. As the field advances, the demands on synchrotron radiation become stricter. To be able to provide synchrotron radiation with the necessary properties, a detailed and complete knowledge of the properties of the electron beam from which the light comes is paramount. For this reason, the development and improvement of measurement techniques dedicated to studying the electron beam are a vital part of operating a synchrotron light source.

The purpose of beam diagnostics at a synchrotron light source is to provide information about the beam as accurately and completely as possible. The longitudinal profile of electron bunches is one property of the beam which can be studied, and is the focus of this thesis. Throughout this work, whenever the term "bunch profile" is used, this refers to longitudinal bunch profiles. Hitherto, bunch profiles have typically been measured using either an optical sampling oscilloscope or a streak camera. Both of these methods come with their own limitations. In the case of the optical sampling oscilloscope, the most obvious limitation is that only one bunch can be studied at a time. The streak camera infers bunch profiles from synchrotron radiation, and is not limited to studying one bunch at a time, as the streak images it creates cover an entire revolution of the ring in time. However, the streak camera suffers from the fact that the light from bunches overlap in the created streak images, acting to "blur" bunch profiles. Furthermore, it is a delicate instrument and is quite sensitive to rapid increases in intensity of incoming light, which makes it unfeasible to use for routine and continuous measurements.

From these and other limitations in present measurement systems stems the need to implement a robust system to measure all bunch profiles in the ring simultaneously and individually, with a sufficient time resolution to resolve longitudinal structure within each bunch. Employing time-correlated single-photon counting (TCSPC), in theory, offers the capability to do so [1, 2]. This thesis is intended to be a first proof of principle with regard to using TCSPC to measure bunch profiles in the storage rings at MAX IV Laboratory.

As a first proof of principle, the work presented in this thesis comes with a number of limitations. These limitations pertain either to the method of implementing TCSPC employed, or to effects which were not taken into account in this work, which, if TCSPC measurements at MAX IV are to be improved in the future, should be. The most important limitation with regard to the implementation of TCSPC as presented in this thesis is the incomplete understanding of the different sources of timing jitter in the system used for measurements. Instead of attempting to account for each relevant component individually, in this work, the main component, the detector TTS was studied, and then an attempt was made to determine the overall timing jitter contribution of the measurement system as a whole. However, there are discrepancies between measurements made to determine the overall system timing jitter, which, while discussed in this thesis, are not yet fully understood.

This thesis is divided into chapters as follows: chapter 2 gives a brief background on the theory underlying synchrotron radiation and longitudinal beam dynamics, as well as a short description of time-correlated single-photon counting. The beginning of chapter 3 is an overview of machine parameters and hardware components used, followed by a discussion of the process of implementing TCSPC to measure bunch profiles at MAX IV and the limitations in said process, the focus being on accounting for the timing jitter produced in the components of the measurement system. The implemented procedure to correct the measured bunch profiles for the system TTS is described. Chapter 4 starts by showing measurements of successfully TTS-corrected bunch profiles from various types of electron beams, highlighting some of the physical properties of the beam that can be observed using TCSPC. The last part of the chapter is dedicated to comparing data obtained from TCSPC measurements to more conventional streak camera measurements. Chapter 5 concludes the thesis and gives an outlook on steps that could be taken to improve on this first implementation of TCSPC to measure longitudinal bunch profiles.

2 Background

The first sections of this chapter are dedicated to outlining relevant parts of accelerator physics. Chapter 2.1 deals with general motion and acceleration of charged particles in electromagnetic fields. Chapter 2.2 is dedicated to the working principles of synchrotrons and storage rings, while Chapter 2.3 discusses some properties of synchrotron radiation relevant to this work. This is followed by an outline of the accelerating radio-frequency (RF) cavities and longitudinal dynamics of the particle beam in Chapter 2.4. The following section, 2.5, describes passive harmonic cavities, and their effect on the longitudinal profile of the beam. The final section of this chapter, 2.6, briefly describes the working principles of TCSPC at a storage ring of a synchrotron light facility.

2.1 Charged particles in electromagnetic fields

The force $\vec{F}$ experienced by a charged particle with charge q and velocity $\vec{v}$ in an electromagnetic (EM) field is the Lorentz force [3], given by

$$\vec{F} = q(\vec{v} \times \vec{B} + \vec{E}), \tag{2.1}$$

where $\vec{B}$ and $\vec{E}$ denote the magnetic and electric fields, respectively. The energy gain ΔE of such a particle between two points $\vec{r}_1$ and $\vec{r}_2$ is given by

$$\Delta E = \int_{\vec{r}_1}^{\vec{r}_2} \vec{F} \cdot d\vec{r} = q \int_{\vec{r}_1}^{\vec{r}_2} (\vec{v} \times \vec{B} + \vec{E}) \cdot d\vec{r} = q \int_{\vec{r}_1}^{\vec{r}_2} \vec{E} \cdot d\vec{r} = qU, \tag{2.2}$$

where U denotes the voltage between $\vec{r}_1$ and $\vec{r}_2$ and the fact has been used that $\vec{v} \times \vec{B} \perp d\vec{r} = \vec{v}dt$. Only electric fields can contribute to linear acceleration, that is, acceleration which changes the energy of a particle.

2.2 Synchrotrons and storage rings as sources of synchrotron radiation

The main idea behind a synchrotron is to achieve higher particle energies E by gradually increasing magnetic field strength B while keeping particles on a circular orbit of constant radius R. This puts a requirement on the relation between E and B, as the Lorentz force (eq. 2.1) must be equal to the centripetal force, giving the bending radius R

$$R = \frac{v\gamma m_0 c^2}{qc^2 B} = \frac{E}{qcB}, \tag{2.3}$$

where $\gamma = (1 - \beta^2)^{-1/2}$ denotes the Lorentz factor and $\beta = v/c$ the speed in terms of the speed of light, m_0 the rest mass of the particle and v its speed. Note that the second equality in eq. 2.3 assumes that particles are highly relativistic, i.e. $v \approx c$ and particle energies $E' \approx m_0 \gamma' c^2$.

A storage ring differs from a synchrotron in that it operates at constant particle energy E and fixed orbit radius R. One immediate consequence of this is that a storage ring cannot be used to accelerate particles to desired energies. To accelerate particles to the desired energy, a pre-accelerator is used. Examples of pre-accelerators include linear accelerators or booster rings. Particles are then injected into the storage ring at the desired energy. The constancy of the radius and particle energy in a storage ring allows for the definition of a ring-specific constant: the revolution frequency f_{rev}, given by

$$f_{rev} = \frac{v}{C}, \tag{2.4}$$

where v denotes the particle speed and C the circumference. To keep particles on the desired trajectory, bending magnets are employed. Bending magnets are usually dipole magnets, as their fields are constant in the horizontal direction, making them useful for deflecting particles along the set near-circular orbit of the ring in the horizontal plane [3]. Typically, the arrangement of magnets is such that there are straight sections between them, meaning that a storage ring is not perfectly circular, but a polygon. While in the magnetic fields of bending magnets, charged particles emit synchrotron radiation, which is discussed in section 2.3. The emission of radiation means that stored particles lose energy while circulating in the ring. To be able to operate the ring at constant energy, particles must have their lost energy resupplied. This is done through the use of accelerating cavities, which are resonators at a specific radio frequency (RF). These cavities are called RF-cavities and are discussed in more detail in section 2.4.

2.3 Properties of synchrotron radiation

While in the magnetic fields of bending magnets, charged particles undergo acceleration in the transverse direction. The corresponding change of momentum causes particles to emit EM radiation, called *synchrotron radiation*, named after the synchrotron. This radiation (light) has a few properties relevant to this work. First is the power P_s radiated by a charged particle during transverse acceleration [3]:

$$P_s = \frac{q^2 c}{6\pi\varepsilon_0} \frac{1}{(m_0 c^2)^4} \frac{E^4}{R^2}, \tag{2.5}$$

where ε_0 denotes the vacuum permittivity. For electrons in a storage ring, the energy loss during one full revolution U_0 is given by [4]

$$U_0 = \oint P_s dt = \frac{C_\gamma E^4}{R}, \tag{2.6}$$

where $C_\gamma = \frac{4\pi}{3} \frac{r_c}{(m_e c^2)^3}$ is a constant, and $r_c = \frac{1}{4\pi\varepsilon_0} \frac{e^2}{m_e c^2}$ denotes the classical electron radius. The loss of energy through emission of synchrotron radiation is the dominant energy loss mechanism for particles close to the relativistic limit. The energy lost is regained in the RF-cavities, which are discussed in section 2.4.

Synchrotron light is emitted in a narrow cone around the tangential direction of the ring in the bending magnets. The opening angle Θ is given by [3]

$$\tan(\Theta) \approx \frac{1}{\gamma}, \tag{2.7}$$

where γ denotes the Lorentz factor. For reference, at electron energies of 3 GeV, this corresponds to an opening angle of $\tan(\Theta) \approx \Theta \approx 0.17$ mrad. In addition to the narrow opening angle, synchrotron radiation is emitted in a broad frequency spectrum, which has a distribution $P(\omega)$ [4]

$$P(\omega) = \frac{P_s}{\omega_c} S\left(\frac{\omega}{\omega_c}\right), \tag{2.8}$$

where $\omega_c = \frac{3}{2}\frac{c\gamma^3}{R}$ is called the critical frequency and $S(\xi)$ is given by

$$S(\xi) = \frac{9\sqrt{3}}{8\pi} \xi \int_0^\infty K_{5/3}\left(\bar{\xi}\right) d\bar{\xi}, \tag{2.9}$$

where $K_{5/3}$ is a modified Bessel function. For reference, at electron energies of a few GeV, the spectrum covers photon energies ranging from infrared (IR) to X-rays. The power of synchrotron radiation is directly proportional to the number of particles in the case that the bunch length is much longer than the wavelength of emitted radiation [5]. This property of synchrotron light becomes important for TCSPC, which is discussed in more detail in section 2.6.

2.4 RF-cavities and longitudinal beam dynamics

As mentioned in earlier sections, electrons in a storage ring will lose energy over time, which is regained in RF-cavities. The RF-cavities considered in this section are active cavities, meaning that power is supplied externally to them, in contrast to passive harmonic cavities, which are outlined in section 2.5. These cavities oscillate at a constant frequency, denoted f_{RF}. Ignoring particle energy loss from sources other than emission of synchrotron radiation, as mentioned in section 2.3, the energy an ideal particle regains in one revolution is exactly U_0, to keep the particle on the ideal orbit. Thus, for an ideal particle,

$$U_0 = eV_{RF}(\Psi = \Psi_s) = eV_0 \sin(\Psi_s), \tag{2.10}$$

where V_0 is the peak voltage in the RF cavity and the phase Ψ_s is called the synchronous phase, and is defined as the phase where an ideal particle regains exactly the energy U_0. One consequence of the fact that the ideal particle reaches the RF voltage at the same phase Ψ_s every revolution is that for stable operation of the beam, the ratio of RF frequency to revolution frequency must be an integer h [3]:

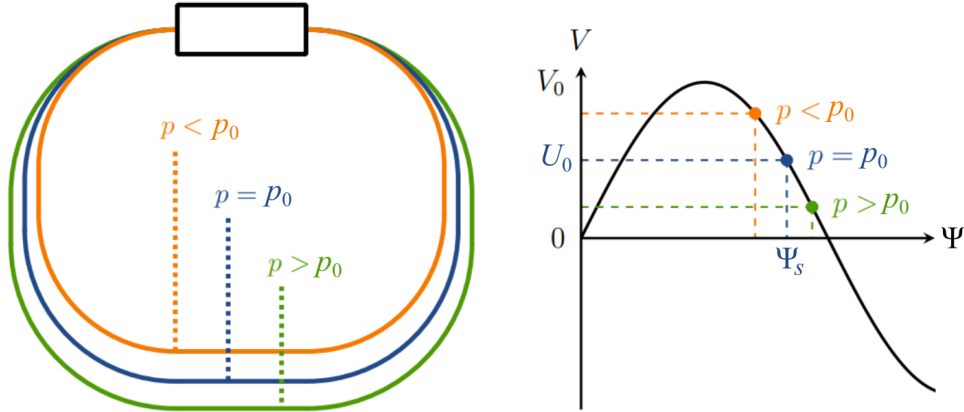$$\frac{f_{RF}}{f_{rev}} = h \in \mathbb{Z}_{>0}. \tag{2.11}$$

3

Figure 2.1: An illustration of phase focusing. Left: particle trajectories in the ring, with positive (green), negative (orange) and zero (blue) momentum deviation. The black box at the top indicates an RF-cavity. Right: A sketch of the RF-voltage experienced by particles depending on phase. Particles with different signs of momentum deviation are indicated the same way as on the left. Reproduced from [6], Figure 2.3.

This number is called the harmonic number and is an important parameter of the beam, as it is equal to the number of stable regions of phase space in the ring, called buckets. For a more detailed but digestible treatment of the longitudinal motion of particles with slight deviations in momentum compared to the ideal particle, see, for instance [3], chapter 5.6, the main results of which will be stated here. Consider a particle with a slight momentum deviation $\frac{\Delta p}{p}$ from the ideal particle momentum p_0. If the momentum deviation $\frac{\Delta p}{p} < 0$, the orbit radius of the particle will be slightly shorter than that of the ideal particle, as can be visualized from eq. (2.3), meaning that it will arrive at the cavity earlier, at a phase $\Psi = \Psi_s - \Delta\Psi$. Because of the phase difference, this particle is subject to a larger voltage in the RF cavity, resulting in a greater acceleration than the ideal particle experiences, acting to restore the initial lower energy of the particle compared to the ideal. The converse holds for particles with a positive momentum deviation $\frac{\Delta p}{p} > 0$; such particles are accelerated less in the cavity. This process continues during subsequent revolutions, leading to a net effect which is called phase focusing, and leads to particles oscillating about the synchronous phase Ψ_s. Particles with different signs of momentum deviation and how the sign of momentum deviation impacts the voltage experienced by a particle in an RF-cavity is illustrated in Figure 2.1, reproduced from [6], Figure 2.3. These oscillations are called synchrotron oscillations, and occur with a characteristic frequency f_s which can be determined by solving the differential equation describing the evolution of the energy deviation ΔE (analogous to the momentum deviation) in time:

$$\Delta \ddot{E} + 2a_s \Delta \dot{E} + \Omega^2 \Delta E = 0, \tag{2.12}$$

where

$$a_s = \frac{1}{2T_0} \frac{dU}{dE}, \tag{2.13}$$

with $T_0 = L_0/v_0$, the revolution time of an ideal particle, U the energy loss of a particle, and Ω the angular synchrotron frequency

$$\Omega = 2\pi f_s = f_{rev} \sqrt{\frac{he}{2\pi \beta^2 E} \left(\alpha_c - \frac{1}{\gamma^2} \right) \frac{dV_{RF}(\Psi)}{d\Psi} \bigg|_{\Psi=\Psi_s}} \tag{2.14}$$

In eq. (2.14), the parameter α_c appears, known as the momentum compaction factor. It is defined via

$$\alpha_c = \frac{\Delta L/L}{\Delta p/p}, \tag{2.15}$$

where $\Delta L/L$ denotes the relative change in path length, and $\Delta p/p$ as before. The momentum deviation Δp, together with the phase difference $\Delta\Psi$ can be used to create a longitudinal phase-space diagram to indicate possible particle trajectories. The trajectory with the highest possible value of $\Delta\Psi$ for which the trajectory is stable is called the separatrix [3]. In a $\Delta p - \Delta\Psi$-diagram, trajectories inside this boundary represent stable synchrotron oscillations, whereas trajectories outside represent unstable oscillations. A
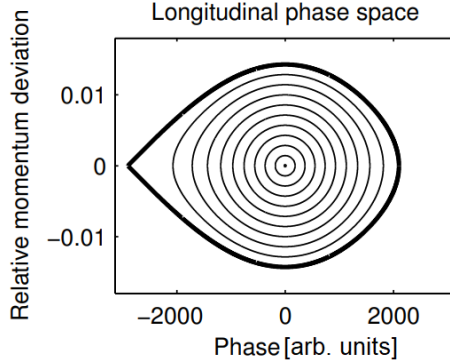
Figure 2.2: A $\Delta p - \Delta\Psi$ phase space diagram showing an example separatrix (thick line) and a number of stable trajectories inside. Reproduced from [7], Figure 5.6.

$\Delta p - \Delta\Psi$ phase space diagram showing the separatrix and stable particle trajectories inside is presented in Figure 2.2. The stable regions are 2π-periodic in the phase difference $\Delta\Psi$, and are called buckets. Consequently, particles in a storage ring are not continuously distributed in real space, but appear in a series of so-called bunches, which correspond to packages of particles stored in the buckets in phase space. The number of buckets throughout the storage ring circumference is given by the harmonic number, as in eq. (2.11).

Particles oscillate in both momentum and phase with respect to the ideal particle. This gives rise to the appearance of a longitudinal distribution of particles [5]. Characterizing this distribution analytically in the general case is highly non-trivial. However, in the limit of low charge, bunches in a ring will appear to have a Gaussian distribution of charge in the longitudinal direction, where the standard deviation of the Gaussian corresponds to the so-called natural bunch length $\sigma_{z,0}$, defined as [5]:

$$\sigma_{z,0} = \frac{c\sigma_{\delta,0}\sqrt{E|\alpha_c|}}{f_{rev}\sqrt{2\pi he \left.\frac{dV_{RF}(\Psi)}{d\Psi}\right|_{\Psi=\Psi_s}}}, \tag{2.16}$$

where $\sigma_{\delta,0} = \sigma_{E,0}/E_0$, where $\sigma_{E,0}$ is the root-mean-square (RMS) of the natural (ideal) energy distribution. Importantly, eq. (2.16) states that in the low-charge (also called low-current) limit, the natural bunch length has a dependence on the peak RF-cavity voltage V_0:

$$\sigma_{z,0} \propto \left(\left.\frac{dV_{RF}(\Psi)}{d\Psi}\right|_{\Psi=\Psi_s}\right)^{-\frac{1}{2}} = (V_0\cos(\Psi_s))^{-\frac{1}{2}}, \tag{2.17}$$

where eq. (2.10) was used in the equality. Equation (2.17) shows that the natural bunch length can be varied by changing the peak RF cavity voltage V_0. At this point it is also useful to state the relationship between full-width at half-maximum (FWHM) of a Gaussian (or normal) distribution and its standard deviation σ:

$$\text{FWHM}_{Gaussian} = 2\sqrt{2\ln(2)}\sigma \approx 2.355\sigma. \tag{2.18}$$

2.5 Passive harmonic cavities

This section is largely based on [7], chapter 5, which gives a comprehensive overview of the functionality of passive harmonic cavities. Passive harmonic cavities, also referred to as (passive) Landau cavities, are similar in function to the active cavities discussed in the previous section. Similarly to the main active RF cavity, Landau cavities operate at a given frequency f_L. This frequency is generally close to the n:th harmonic of the fundamental RF frequency. Throughout this section, only higher harmonic cavities will be considered, i.e. $n > 1$. The relation between the main RF frequency and the Landau cavity frequency is thus

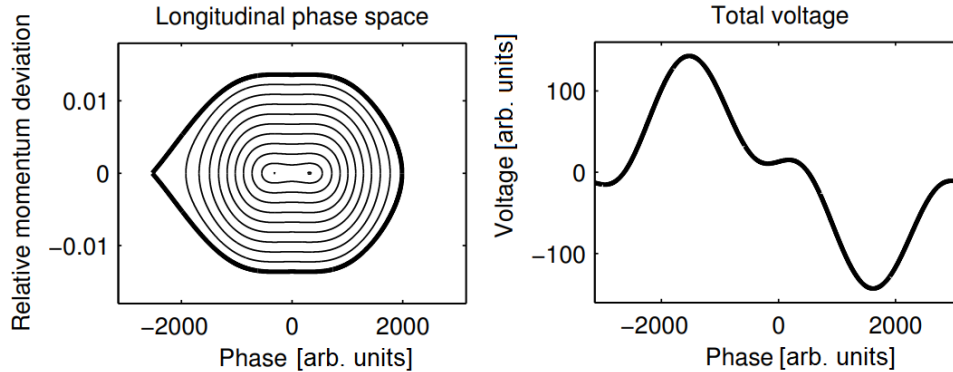$$f_L \approx nf_{RF}, \ n \in \mathbb{Z}_{>1}. \tag{2.19}$$

5

Figure 2.3: Left: A $\Delta p - \Delta \Psi$ diagram, indicating the separatrix in case of high beam current. Note the emergence of two minima in phase space. Right: The total voltage experienced by particles in the beam; a combination of the main RF voltage and the voltage induced in the Landau cavities by passing electrons. Reproduced from [7], Figure 5.13.

The main difference between active and passive cavities is that passive cavities are not powered by an external power source, but by the beam itself [7]. The basic working principle is as follows. Electrons in a bunch travel through the passive harmonic cavity. In the cavity, the electrons lose some energy U_L and induce an electric field, and with it, a voltage V_L through the cavity. Electrons in subsequent bunches traversing the same cavity experience the field left behind, while themselves contributing to it. A consequence of this is that the effect of Landau cavities are emphasized for beams containing a lot of charge (current). The net effect of electrons depositing energy and changing the electric field accordingly is that the effective total voltage in a region around the synchronous phase Ψ_s changes [7]. Typically, Landau cavities are used in this way to reduce the slope of the potential $\frac{dV_{RF}(\Psi)}{d\Psi}\Big|_{\Psi=\Psi_s}$, which leads to longer bunches (similar to eq. 2.16). For a given beam current, longer bunches correspond to a lower electron density in a given bunch, which can increase the lifetime of the beam [7].

The right-hand diagram in Figure 2.3 shows how the effective voltage experienced by particle bunches can change in the presence of Landau cavities compared to the sinusoidal main RF-potential as given by 2.10. The left-hand diagram shows the effects such a potential has on the possible stable trajectories of particles in a $\Delta p - \Delta \Psi$ diagram. Note that in the Figure, phase is indicated relative to the synchronous phase, meaning that in horizontal axis labels, "phase" refers to $\Delta \Psi$ as before. Notably, the potential on the right in Figure 2.3 has two stationary points at a region around $\Delta \Psi = 0$, which leads to two extrema in phase space. In real space, this is reflected by a bunch profile with two distinct peaks, rather than the natural Gaussian distribution [7].

The case where all bunches contain close to equal charge is the simplest when considering Landau cavities. This situation is called a homogeneous fill pattern. In general, the term fill pattern refers to the distribution of charge in the different buckets. In the case of a homogeneous fill pattern, the voltage in the cavity does not change significantly as different bunches pass it, meaning that all bunches are affected the same way. The case of an inhomogeneous fill is different. Such a fill can be obtained by emptying (partially or close to fully) specific buckets in a process known as *scraping*. Another method of creating an inhomogeneous fill when there is no current in the ring is to only inject electrons into specific buckets, leaving some with less charge or even empty. An inhomogeneous fill leads to different effects when subject to Landau cavities, as in this case individual bunches see a different field depending on the amount of charge in the bunches before. One such effect is a gradual shift of relative phases between bunches when a *gap* (a series of consecutive empty buckets, at least one) is introduced into the fill pattern [8]. This effect is known as a phase *transient*.

2.6 Measuring bunch profiles using time-correlated single-photon counting

This section will outline how the method of time-correlated single-photon counting (TCSPC) will be employed within the scope of this thesis to measure bunch profiles at a storage ring. For TCSPC to

be viable, one property of synchrotron light itself must be considered, namely that the power (and by extension the intensity, or number of photons) of synchrotron light should be directly proportional to the amount of emitting charge (effectively the number of electrons) [1]. This is the case for incoherent synchrotron radiation [5]. As mentioned in section 2.3, the criterion for synchrotron radiation to be incoherent is that the bunch length is much longer than the wavelength of the light considered.

To perform TCSPC, two hardware components are necessary. First, a single-photon detector. Second, a device to sort arrival times of single-photon detection events relative to a trigger. A convenient choice of trigger is the revolution clock. To sort photon detection events relative to the revolution clock, a histogramming device is ideal, as it can count the number of events with a given time difference between the revolution clock and photon detection event [2]. With this measurement method and the fact that the number of emitted photons is directly proportional to the number of electrons, given a sufficiently long measurement (integration) time, bunches in the ring are reconstructed in the histogram as regions with high counts. This approach is often used to measure the relative distribution of charge in the different bunches, the so-called fill pattern. Given sufficient resolution of the histogramming device, even intra-bunch structure can be measured. Thus, TCSPC, in principle, has the ability to measure the bunch profile of each bunch simultaneously. In reality, there are a few more considerations for the successful implementation of TCSPC. The first consideration is the count rate, that is, the number of counts per unit time the histogramming device receives. A count rate exceeding the revolution frequency leads to dead-time effects of the histogramming device and measurement pile-up [1, 2]. Thus, ensuring that the count rate does not exceed the revolution frequency is paramount to obtain accurate data. For more details on dead-time effects and a possible compensation scheme, see for instance [9].

In addition to considerations with regard to the count rate, the properties of the hardware must be taken into consideration, particularly timing jitters. Ideally, the method outlined above would give accurate representations of bunches in time. However, due to jitter in the various timing signals used, this will not directly be true. Each of the signals comes with its own jitter, or transit time spread (TTS): the revolution clock signal; the detector; the intrinsic timing jitter of the histogramming device. The combined effect of these three jitter contributions will throughout this thesis be referred to as the total system TTS, or system TTS. To obtain accurate bunch profile measurements, the total system TTS needs to be accounted for. The process of characterizing the system TTS, and to implement a method of recovering bunch profiles from histogram bunches is discussed in sections 3.6 and 3.7, respectively.

3 Experimental setup and procedure

This chapter aims to give an overview of the procedure taken to implement TCSPC at the two rings at MAX IV Laboratory, the focus being on determining the overall system jitter and compensating for it. Section 3.1 gives a general overview of the components used and how they interact. Section 3.2 gives an overview of the detector setup. Section 3.3 discusses the hardware components in more detail, as some of their properties are crucial to the process. The section thereafter, 3.4, deals with the wavelength sensitivity of the measurement setup, in particular the detectors. The next section, 3.5, measurements made to determine the detector TTS directly are described in some detail. The discussion of detector TTSs is directly followed by a description of the measurements made to determine the TTS of the system as a whole in section 3.6. The final section of the chapter, section 3.7, briefly describes how bunches are deconvolved using the system TTS, showing the impact on an example bunch.

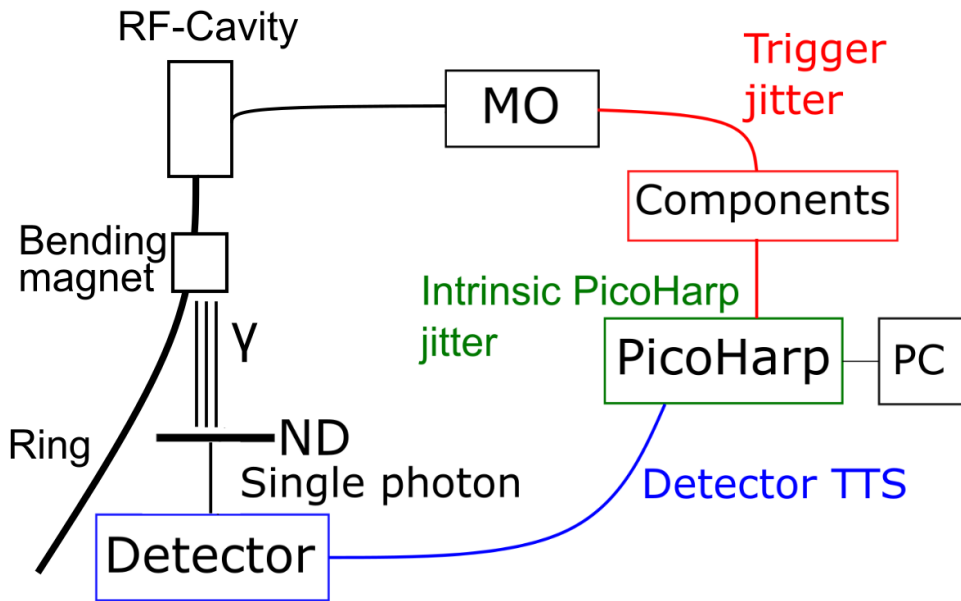## 3.1 Overview of the TCSPC setup at MAX IV

Figure 3.1: A schematic of the TCSPC setup used at the storage rings at MAX IV.

Figure 3.1 depicts a schematic of the TCSPC setup used at each storage ring at MAX IV Laboratory. The component labeled "MO" at the top is the master oscillator, which both drives the RF-cavities, labeled by a box, and gives a signal acting as a revolution clock to the histogramming device (PicoHarp). The revolution clock signal, labeled in red in Figure 3.1, passes through a series of components ensuring its compatibility with the histogramming device. The components add jitter to the signal, labeled "trigger jitter". On the left side of Figure 3.1, the photon detection scheme is depicted. Synchrotron light is obtained from a bending magnet. To reach the single-photon regime, neutral density (ND) filters are used to ensure that the count rate does not exceed the revolution frequency. The spectral bandwidth of synchrotron radiation from the bending magnet is broad, ranging from X-rays to infrared (IR) light. X-rays are filtered out using mirror surfaces of SiC and transmission optics lens made from fused silica, leaving light in an approximate wavelength range of 250 nm to 1200 nm to reach the detector. Furthermore, the detector performance is wavelength-dependent, which is addressed in section 3.4. As will be discussed in later sections of this chapter, the detector TTS is the single largest contribution of jitter to the system. In fact, the detector TTS is in some cases a longer (in time) signal than the bunch profile itself, which highlights the need to determine the total system TTS. As outlined in 2.6, bunches can then be deconvolved using said system TTS, to obtain a measurement of bunch profiles as accurate as possible. It is also worth mentioning that each setup has a streak camera, which is another device that can be used to measure bunch profiles in the ring using synchrotron radiation. As the purpose of this thesis is to act as a proof of principle for using TCSPC to measure bunch profiles at MAX IV in a robust and
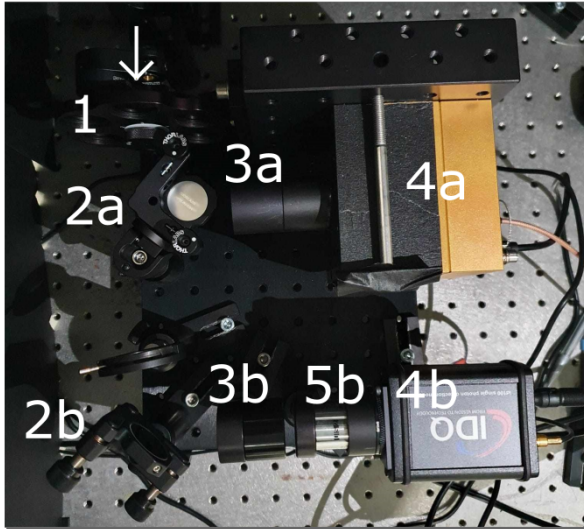
Figure 3.2: A top-down photo of the detector breadboard used for measurements at the beamline, with labeled components. The arrow in the top-left corner indicates the direction of incoming synchrotron light.

reliable way, it is meaningful to compare measurements made using TCSPC to those made by the more conventional streak camera, which is done in chapter 4.

MAX IV Storage rings

The synchrotron light facility at MAX IV Laboratory has two electron storage rings, called R1 and R3. Both have the same main radio frequency (RF), 99.931 MHz. R1 is the smaller of the two, with a circumference of 96 m and stores electrons at an energy of 1.5 GeV. Its harmonic number is $h_{R1} = 32$ and the revolution frequency is $f_{rev}^{R1} \approx 3.125$ MHz. R3 has a circumference of 528 m, electrons are stored at 3.0 GeV and the harmonic number is $h_{R3} = 176$ and its revolution frequency $f_{rev}^{R3} \approx 0.5682$ MHz. In terms of finding the total system TTS, each ring is treated as a separate system. Each ring has a beamline dedicated to beam diagnostics [10], which is where the setup was used. It is also worth noting that due to the relatively lower revolution frequency at R3, count rates at R3 need to be lower than at R1. To achieve similar statistics in terms of total counts between the two rings, integration times need to be longer at R3.

3.2   Overview of the detector setup

The experimental setup consists of an optical breadboard for the photon detectors, and a histogramming device, or TCSPC module, namely a PicoHarp 300, manufactured by PicoQuant. The optical breadboard is assembled in a way to simplify switching which detector to use between measurements. Referring to Figure 3.2, the labels denote different components: (1) A filter wheel with different neutral density (ND) filters, which allows varying the count rate between measurements; (2a-b) micrometer-scale adjustable flip mirrors. Each mirror is adjustable both horizontally and vertically, used for alignment. Flipping mirror 2a changes which detector receives synchrotron light; (3a-b) Optical bandpass filters; (3a) has a central wavelength of 488 nm and a width of 10 nm, while (3b) has a central wavelength of 405 nm and a width of 5 nm. Both optical bandpass filters are manufactured by Edmund Optics; (4a-b) The photon detectors; (4a) A PMA 175 photomultiplier detector assembly, manufactured by PicoQuant; (4b) An ID100 single-photon avalanche diode (SPAD), manufactured by IDQuantique; (5b) a focusing objective to focus synchrotron light on the SPAD. It is worth pointing out that the entire detector breadboard is encased in a box while on the optical table, to minimize the amount of background light.

3.3   Hardware components

PicoHarp 300

The PicoHarp acts as a histogramming device. It has two input channels. The first, Channel 0, is used as a starting trigger, while the other, Channel 1, acts as a stopping trigger. For most measurements, the revolution clock signal is used as the Channel 0 trigger. The device bins the time difference between the trigger signal from input Channel 0 and the signal from input Channel 1, while the vertical axis counts the number of events. Histograms created by the PicoHarp have a maximum of $2^{16} = 65536$ bins, while the bin width is adjustable through software in factors of 2, with a base width of 4 ps. The number of bins in a histogram limits the minimum bin width at each ring to be able to cover one revolution in time. These minimum bin widths to cover one revolution are 8 ps at R1 and 32 ps at R3. The minimum bin width also limits the resolution of the system, and as such measurements at R3 will always have worse resolution than measurements at R1. Furthermore, the PicoHarp has an intrinsic timing jitter which will contribute to the overall system TTS. A measurement was made to determine the width of this jitter, by splitting the revolution clock signal, and connecting the cable ends to each of the PicoHarp's input channels. This resulted in a histogram showing a single peak, which had a FWHM of about 21.5 ps. As will be discussed in the coming sections, this is a small contribution to the overall system TTS compared to the intrinsic detector TTSs.

ID100 single-photon avalanche diode

There are a few properties of the ID100 single-photon avalanche diode[1] (SPAD) that should be highlighted within the framework of this thesis. The first is the active area, which has a diameter of 20 μm. This small area necessitates the use of the focusing lens and micrometer-scale adjustable mirrors, as shown in Figure 3.2. The manufacturer states the timing resolution is optimized when incoming light is focused on the active area. A thorough characterization of this effect is outside the scope of this project. The SPAD also has an intrinsic timing jitter (or transit time spread, TTS), which will be reflected in the histograms produced by the PicoHarp. The detector TTS is a measure of the jitter in the time difference between a photon striking the detector and the detector giving an output signal. Manufacturers give a value of this jitter at FWHM of <60 ps, typically 40 ps.

PMA 175 Photomultiplier detector assembly

The other detector used for measurements is a PMA 175 Photomultiplier assembly[2] (PMA), manufactured by PicoQuant. With regard to detecting photons, the detector is effectively a photomultiplier tube. Compared to the SPAD, the active area of the PMA is large, at a diameter of about 8 mm, which means that this detector has the advantage that measurements are not as sensitive to beam position. The manufacturer gives a typical value of the intrinsic TTS of the PMA in FWHM of <180 ps.

3.4   System sensitivity to wavelength

Another property to consider is the detector response to the wavelength of incoming light. One factor to consider is that the photon detection efficiency is wavelength-dependent for both detectors, meaning that for incoming white light, the count rate can change by a factor of up to 10 when using different optical bandpass filters for the SPAD and a factor of up to 100 for the PMA. This effect can be accounted for by changing the ND optical filter accordingly.

For both detectors, it was investigated whether the histograms created by the PicoHarp would change depending on wavelength. To do this, measurements were performed parasitically on the beam during normal operation, where the beam is kept as stable as possible, while leaving the setup unchanged except for the optical bandpass filter in front of the detector. Due to the PicoHarp being triggered by a revolution clock, provided the beam does not change, bunches appear in the same position in every histogram. Thus, the shape of one particular bunch can be examined from different histograms, as it appears in the same

---

[1] https://www.idquantique.com/quantum-sensing/products/id100/
[2] https://www.picoquant.com/products/category/photon-counting-detectors/pma-series-photomultiplier-detector-assembly
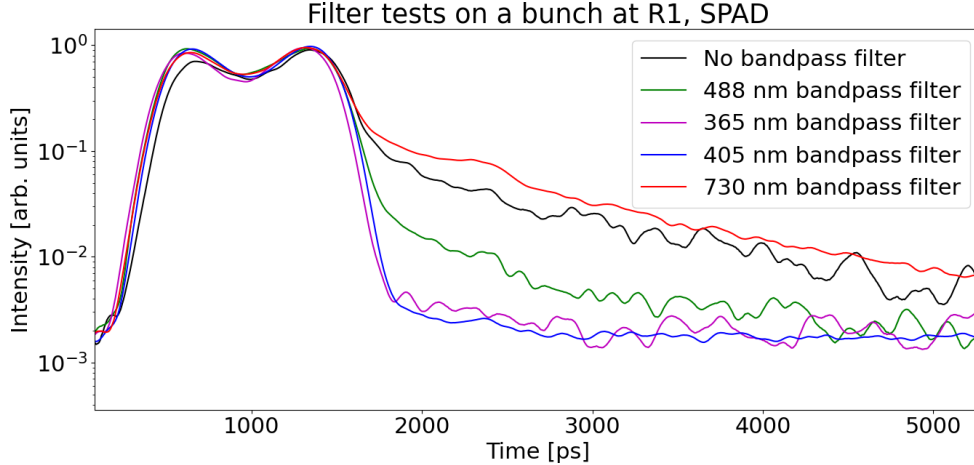
Figure 3.3: A bunch at R1 measured using the SPAD detector and five different optical bandpass filters. Note that the vertical axis is in logarithmic scale. The data has been smoothed using a moving average. Note that the colors used to label the different curves do not correspond to the wavelengths given in the legend.

spot in every histogram. For the PMA, no significant difference was found when using optical bandpass filters with central wavelengths in the region of 400-500 nm. For further measurements, a bandpass filter with a central wavelength of 488 nm and a width of 10 nm was chosen.

The case of the SPAD is different. Figure 3.3 shows the same bunch from five different measurements, each made using a different optical bandpass filter. While the widths of the bunch in the histogram do not change significantly with wavelength, the bunch profiles after the main peak(s) are different when using different optical bandpass filters. In the case of a red 730 nm bandpass filter, a "tail" appears after the main peak which is significantly above the noise, similar to the case where no bandpass filter is used. This effect is still visible but not as pronounced for a 488 nm bandpass filter, and is minimized when using a 365 or 405 nm filter. The fact that all parameters were kept constant except the bandpass filters used indicate that the SPAD TTS is wavelength-sensitive. In the interest of minimizing detector TTS, it was decided that the 405 nm, width 5 nm bandpass filter would be used for all further measurements using the SPAD detector.

3.5 Characterization of detector TTSs using laser pulses

The intrinsic detector TTS is one of the contributing sources to the overall system TTS at the rings. In this section, a discussion about how detector TTSs were measured directly will be given. These measurements were performed with the PicoHarp. As mentioned in section 3.3, the intrinsic jitter of the PicoHarp comes to about 21.5 ps at FWHM, which is small compared to the expected detector TTSs (for SPAD and PMA <60 and <180 ps FWHM, respectively, see section 3.3). To measure the intrinsic detector TTS directly, timing jitter from all other sources must be minimized. For one, this means that a more direct trigger chain involving fewer components each with their own intrinsic jitter should be used. The other question is what to measure. The idea here is to measure a pulse of light which is short compared to the detector TTS. In combination with a more direct trigger chain, the detector TTS becomes the dominant contribution to profiles in the histogram, meaning that detector TTSs can be read out directly from the histogram. This neglects the intrinsic PicoHarp jitter, but as will be seen, its contribution is relatively small.

Short laser pulses are ideal for this purpose. The laser lab at MAX IV is capable of producing periodic laser pulses with lengths on the order of 100 fs. Hence the setup was moved to the laser lab, to carry out measurements of this kind. Moreover, the trigger scheme was simpler than at the rings; the Channel 0-trigger of the PicoHarp was connected to the oscillator driving the laser, such that the timing in the histogram was correlated to the laser pulses, resulting in an expected jitter of a few ps. The main
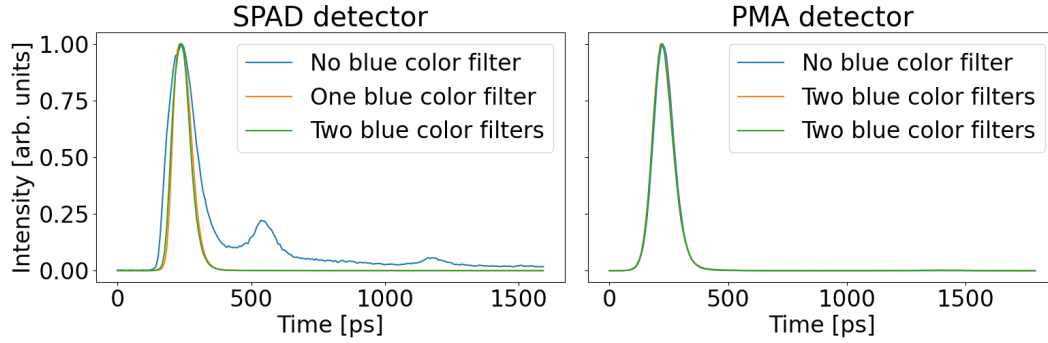
Figure 3.4: Short laser pulses measured with the PicoHarp and different detectors. Left: pulse measured using the SPAD detector. Right: pulse measured using the PMA detector. Note that the vertical axis is the same for the two plots.

contributing jitter sources at this setup are: detector TTS; intrinsic PicoHarp jitter (21.5 ps FWHM); trigger signal jitter (expected to be a few ps); laser pulse width (order 100 fs). The intrinsic detector TTS is thus expected to be the single largest contribution to the shape of pulses measured in the histogram. The most significant problem with this setup was the fact that the laser pulses consisted mostly of 800 nm infrared (IR) light. As discussed in section 3.4, the SPAD and PMA detectors are combined with optical bandpass filters with central wavelengths of 405 and 488 nm, respectively. As the detectors were going to be used in conjunction with their respective chosen bandpass filters, the wavelength of laser light had to be changed. For this purpose, a crystal was used to double the frequency of the laser beam into 400 nm blue light. Still, the relative intensity of IR to blue light was about three to four orders of magnitude more IR than blue photons. To account for this, different measurements were taken employing a varying number of wide (in terms of bandwidth) optical bandpass filters with central wavelengths of about 450 nm. Each blue color filter is expected to attenuate IR light by about 3 orders of magnitude each. It should be noted that the narrow bandpass filters in front of each detector were still in place during laser measurements.

Using these measurements, a comparison can be made between the values of the measured FWHM of the main peak in each TTS and the corresponding values given by the manufacturers. As mentioned in section 3.3, the FWHM of detector TTSs given by the manufacturers are <60 ps for the SPAD, and <180 ps for the PMA. While the data from laser measurements, presented in Figure 3.4, is consistent with manufacturer claims for the PMA, with FWHM of <100 ps, the measured FWHM of the SPAD TTSs are wider than those claimed by manufacturers. In the case of no blue filter, the FWHM is about 122 ps, and in the case of one or two blue filter, the FWHM is < 80 ps. Figure 3.4 shows that the SPAD TTS is sensitive to wavelength, not just in terms of FWHM, but also in terms of the overall shape of the TTS, as two smaller peaks appear, at time separations of about 350 ps and 1 ns w.r.t. the main peak. The right-hand plot in Figure 3.4 shows the TTSs inferred from laser measurements using the PMA detector. These are consistent with each other, both in terms of FWHM and overall shape, indicating that PMA TTS is not strongly wavelength-dependent, at least when the PMA receives IR vs. blue light. A notable feature when comparing the TTSs of the two detectors to each other is that the SPAD when using at least one blue filter has a TTS which has a main peak with FWHM that is roughly 20 ps, or 20%, narrower than that for the PMA. Determining the reason for the difference in main-peak FWHM between the detectors is outside the scope of this project, but the result that the SPAD TTS is narrower than the PMA TTS is kept in consideration. In particular, for any given bunch, it is expected that it appears longer when measured using the PMA than when using the SPAD.

3.6 Characterization of system TTSs using low-current measurements

The purpose of the setup is to be used at the rings. Each combination of ring and detector is treated as a distinct system, with its own system TTS to be determined. That is, determining the convolution of detector TTS, trigger signal jitter, and intrinsic PicoHarp jitter using data from the PicoHarp. The main remaining contribution to profiles as seen in histograms is the bunch profile itself. A known bunch profile can be used to calculate the system TTS, by deconvolving the histogram bunch with the known bunch profile. This is the idea behind using low-current measurements to determine the system TTS, as when operating the rings in the low-current limit, as outlined in section 2.4, the bunch profiles approach
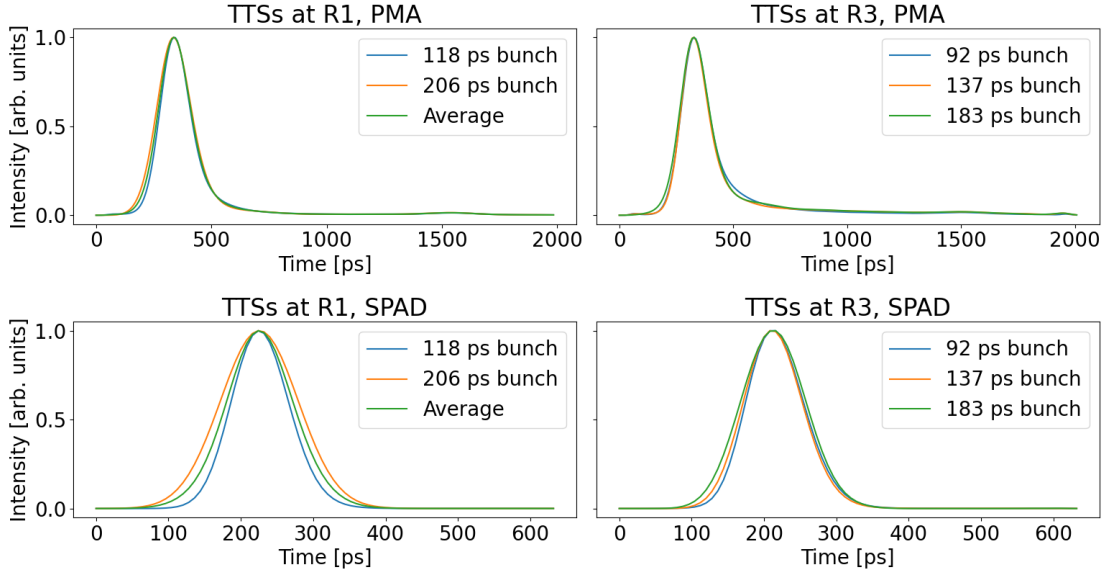
Figure 3.5: System TTSs, measured at each ring using each detector. The times in legends are a measure of the FWHM of the Gaussian bunches used for deconvolution, as measured by the streak camera. Across each row, the vertical axis is the same. Note that data from R3 has been interpolated before deconvolution.

a Gaussian shape, with a length (effectively the standard deviation σ of the Gaussian profile) that can be measured using a streak camera. The bunch length can be varied by changing the main RF-cavity voltage, as outlined in section 2.4. The detector TTSs are assumed to not depend on bunch profiles, as the detectors are single-photon detectors and should thus not be able to distinguish between photons emitted from regions with higher or lower charge. The same assumption is made about jitter in the other components.

The point of performing these measurements is the determination of the total system TTSs. Once determined for each combination of ring and detector (for a total of four system TTSs), these are used to determine bunch profiles from raw histogram data. Now, the script used to perform the deconvolution to find the system TTS will be outlined. The procedure is as follows: it identifies bunches in the histogram by finding regions significantly above the noise. In addition to the histogram, a further input is required, namely a bunch length, the value of which is measured using a streak camera. This value is a measure of the FWHM of bunches, and as bunches profiles are approximately Gaussian in the low-current limit, the FWHM can be used to calculate the standard deviation of the corresponding Gaussian, via eq. (2.18). This allows to create an array representing the bunch profile, as the mean and amplitude of the assembled Gaussian are of no significance. Each bunch recovered from the histogram is then deconvolved using the created Gaussian profile, giving TTSs as inferred from individual bunches. Deconvolution is carried out using the scikit-image-module of the Richardson-Lucy algorithm[3]. Typically, the Richardson-Lucy algorithm is used for image restoration. It takes two inputs: a signal to be sharpened (a bunch in the histogram), and a point spread function (PSF), which in this case corresponds to the estimated bunch profile. Through a series of iterations the algorithm sharpens the signal. For further details, please refer to the original paper on the algorithm by Richardson [11]. A number of Python modules for deconvolution were tested, and the Richardson-Lucy algorithm was chosen for its numerical stability and relative insensitivity to noise compared to other modules. Once the bunch-specific TTSs are determined, they are averaged over all bunches, giving the final system TTS.

There are two important remarks to be made on this procedure. The first remark is that data from R3, while suffering from inherently worse resolution, provides more statistics in the sense that it contains information from more bunches, 176 compared to 32 at R1. The second remark pertains to the issue of resolution. As mentioned earlier, the minimal bin width of the histogram to be able to cover one revolution in time is different between the rings, at a value of $8\,\mathrm{ps/bin}$ at R1 and $32\,\mathrm{ps/bin}$ at R3. At R3, in combination with the fact that there are more bunches, this limits the time resolution within a

---

[3]https://scikit-image.org/docs/stable/auto_examples/filters/plot_deconvolution.html
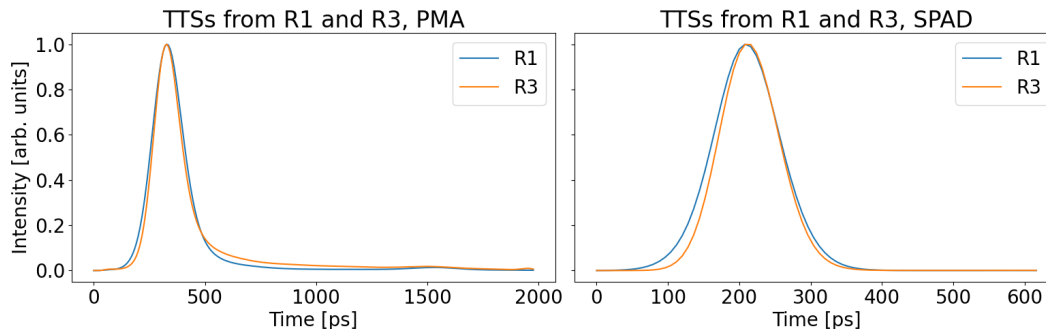
Figure 3.6: Comparison of system TTSs between R1 and R3 for each detector. Note that the vertical axis is the same across both plots.

bunch, as each bunch is represented by fewer data points compared to R1. The deconvolution algorithm is sensitive to this lack of statistics, as it determines TTSs from each bunch individually. It was deemed necessary to account for this sensitivity, which is done by interpolating data from R3 using a cubic spline interpolation, which returns interpolated data points at intervals of effectively 8 ps, the same as for R1.

The determined system TTSs are shown in Figure 3.5. In opposition to the assumption that TTS does not depend on bunch profile, the TTSs obtained for a given ring differ slightly for different bunch lengths. Tendentially, for a given ring and detector, the TTSs obtained from longer bunches are wider than those obtained from shorter bunches. The effect is most pronounced at R1 when using the SPAD detector. The FWHM of the system TTS obtained from the shorter 118 ps bunches is about 93 ps, while the same for the 206 ps bunches is 126 ps.

There are a few possible reasons for this, some of which pertain to the streak cameras. At this point it should be mentioned that two different streak cameras were used, one at each ring. These are configured in slightly different ways, and should not be assumed equal. One factor contributing to the inaccuracy of streak camera measurements is noise. Due to these measurements being taken in the low-current limit of the beam, the signal-to-noise ratio is low compared to the high-current case, which translates to streak camera data being particularly noisy. The low-current nature of measurements bring about another factor to consider. Due to the relatively low intensity of light reaching the streak camera, integration times needed to be rather long. As discussed in section 2.4, bunches oscillate about an ideal phase. The long integration times averages measurements over many such oscillations, which leads to a general overestimation of bunch lengths. This effect, while being present for all bunches regardless of length, relatively affects shorter bunches more. This could act as a partial explanation to the phenomenon observed in Figure 3.5, as if short bunches are even shorter, the system TTS obtained from the short bunches becomes longer.

A comparison can be made between TTSs obtained from the different rings for a given detector. Figure 3.6 shows the average TTSs from Figure 3.5 overlayed for a given detector. The system TTSs when using the SPAD are similar in shape, but have slightly different widths, at $\text{FWHM}_{SPAD}^{R1} = 108$ ps, $\text{FWHM}_{SPAD}^{R3} = 97$ ps. The case of the PMA in terms of width, $\text{FWHM}_{PMA}^{R1} = 164$ ps, $\text{FWHM}_{PMA}^{R3} = 145$ ps. There is, however, a noticeable difference in shape in the case of the PMA, as the R3 TTS does not decrease as rapidly as the R1 TTS in time. The reason for this is not known. For both detectors, the system TTS obtained at R3 is narrower than at R1. It should be pointed out that each configuration of ring and detector is a distinct system. Within the framework, the most relevant differences between the rings are: the different component chains from which the PicoHarp's trigger signal comes from the MO; differences in light due to different bending radii and electron energies; different streak cameras. Thus, each configuration of ring and detector is viewed as a distinct system, each with a distinct system TTS, as presented in Figure 3.5. These TTSs are used to obtain the results, presented in section 4.
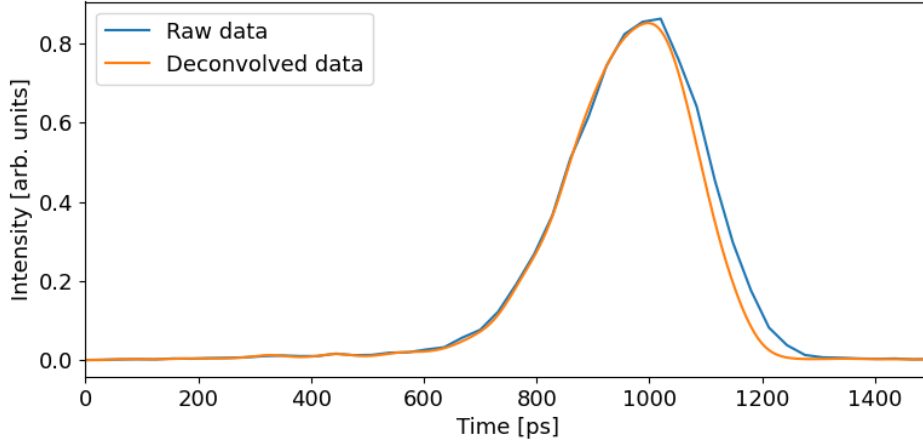
Figure 3.7: A plot of a bunch profile measured from an inhomogeneous fill pattern at a current of 400 mA at R3 using the SPAD detector before and after deconvolution. The data has been interpolated before deconvolving, and the deconvolved profile has been shifted to overlap with the raw profile.

3.7 Finding bunch profiles using deconvolution of histograms

The process of finding bunch profiles once the TTSs have been established is very similar to the process of finding the system TTSs themselves. In effect, the only change is that instead of deconvolving histogram bunches with a "known" bunch profile to obtain the total system TTS, the histogram bunches are deconvolved with the system TTSs as shown in Figure 3.5 to obtain the bunch profiles. Again, the scikit-image module of the Richardson-Lucy algorithm was used for the deconvolution of bunches, and data from R3 was interpolated due to the limited resolution discussed in section 3.6.

As an example of a deconvolved bunch, Figure 3.7 shows a bunch profile measured at R3 with the SPAD detector. It can be seen that the shape of the profile is rather symmetric, and that the deconvolution does not change the shape significantly. This is expected, since the system TTS used for deconvolution is itself rather symmetric (Figure 3.5 for reference). The most notable difference is that the deconvolved bunch is shorter, at $\text{FWHM}_{deconvolved} \approx 260\,\text{ps}$, compared to $\text{FWHM}_{raw} \approx 278\,\text{ps}$. The bunch presented in Figure 3.7 is rather long, and it should be expected that deconvolution has a more pronounced impact on shorter bunches.

4 Results

This chapter is dedicated to showcasing measurements made with the PicoHarp and how the deconvolution of histogram bunches may affect the measurement. Sections 4.1 to 4.3 discuss measurements of various fill patterns using different combinations of detector and ring. The chapter begins with section 4.1, which discusses a measurement made of a homogeneous fill pattern in the low-current limit. The next section, 4.2 considers a measurement of a high-current homogeneous fill pattern. Thereafter, section 4.3 deals with the case of an inhomogeneous fill pattern in the high-current case. The last section of the chapter, 4.4, is a slightly more detailed comparison of streak camera data and PicoHarp data, in an effort to compare the established measurement method of determining bunch profiles to the method based on TCSPC developed in this work.

4.1 Bunch profiles in a low-current homogeneous fill pattern

This section is dedicated to showing the effect of deconvolving histogram bunches in the case of a low-current homogeneous fill pattern, arguably the simplest fill pattern to consider. Presented in Figure 4.1 are bunch profiles measured in a low-current (3 mA) homogeneous fill pattern at R1 using the PMA detector.
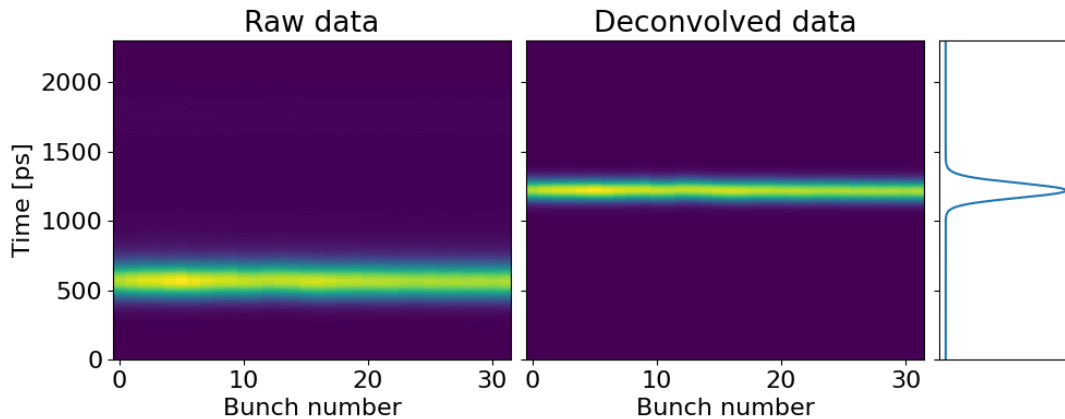

Figure 4.1: A measurement of bunch profiles in a low-current (3 mA) homogeneous fill pattern at R1 measured with the PMA detector. To test the deconvolution algorithm, the PMA detector was chosen, as its TTS is wider than that of the SPAD. The vertical axis is the same for the three plots. The profile on the right-hand side is the average bunch profile after deconvolution. The bunch peak positions have been shifted as a result of deconvolution.

In the plots, each bunch is represented by a column, with brighter color corresponding to a greater amount of charge. The horizontal axis indexes the bunches. The data on the right is equivalent to a part of a histogram where all bunches have been interpolated and deconvolved with the algorithm described in section 3.7. This type of 2D-plot is useful to show the entire fill pattern in one figure, and is used throughout this chapter for this purpose. It should be noted that the range of the vertical axis does not correspond to $1/h_{R1} = 1/32$ of the total revolution time $T_{R1} = 1/f_{rev}^{R1} = 320$ ns. For clarity, a large part of the empty regions between buckets have been left out of the plot.

Considering the plots in Figure 4.1, there are mainly two distinguishing features between the plots. Firstly, the deconvolved bunches are shorter than bunches in the raw data, which is the desired effect, as the contribution to bunch length from the system TTS has been removed. Secondly, the center positions of bunches in time have been shifted in the process of deconvolution. This effect, while pronounced, does not alter any of the desired information within the scope of this work. The reason for this is that within this work, the interest is in properties of bunch profiles with respect to each other. The time $t = 0$ in a histogram is arbitrary, and so a close to constant (given that the same system TTS is used for the deconvolution of all bunches) shift in time does not entail a loss of information.
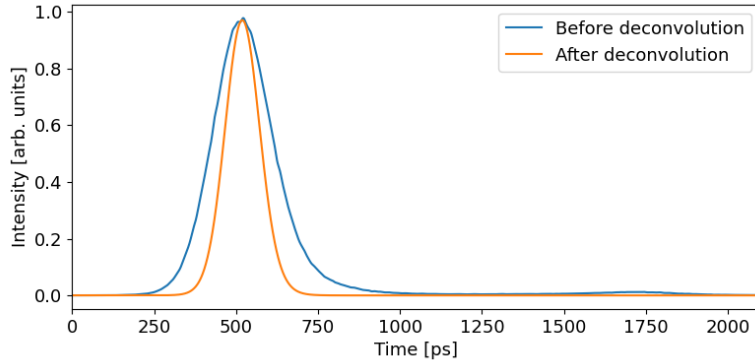
Figure 4.2: A bunch profile from the fill pattern presented in Figure 4.1. Note that the deconvolved profile has been shifted to overlap with the raw profile for clarity.

To obtain a more detailed view of the effects of deconvolution on a bunch profile, in particular when employing the PMA detector, consider Figure 4.2. The width of the raw bunch profile is $\text{FWHM}_{raw} = 208\,\text{ps}$, while the width of the deconvolved profile is $\text{FWHM}_{deconvolved} = 125\,\text{ps}$. The bunch length was also measured using a streak camera. This measurement gave a value of $\text{FWHM}_{streak} = 116\,\text{ps}$. The deconvolution brings the bunch lengths significantly closer to the value measured with the streak camera, but the measured bunch lengths are not in perfect agreement. Likely, this is due to the system TTS for the PMA at R1 being too narrow. One possible reason for this was mentioned in section 3.6, namely that the streak camera measurements are integrated over many synchrotron oscillations, which leads to a general overestimation of bunch lengths. As bunch lengths obtained from streak camera measurements were used to determine system TTSs, it is likely that the widths of system TTSs are generally underestimated somewhat. One possibility to correct for this would be to account the streak camera data for synchrotron oscillations, leading to slightly shorter measured bunches, and in turn slightly wider system TTSs. An investigation of implementing such a correction, and to see its effect on obtained system TTSs is something yet to be done, and is thus a limitation of this work. It is also possible that the overestimation of bunch lengths is a detector- or ring-specific phenomenon. As is covered in section 4.4, a measurement of a fill pattern using the SPAD detector at R3 gave consistently shorter bunch lengths than the streak camera measuring the same fill in parallel. It is also worth pointing out that the small peak at about 1700 ps in Figure 4.2, or about 1.2 ns after the main bunch, is removed when deconvolving. While this peak is expected to appear in a raw histogram, as it stems from the system TTS (see Figure 3.5 for reference), Figure 4.2 indicates that the deconvolution algorithm is capable of removing this artefact.

4.2 Bunch profiles in a high-current homogeneous fill pattern

This section is dedicated to more closely examining a bunch profile in the case of a high-current (approximately 400 mA) homogeneous fill pattern, which resembles the conditions during routine operation at MAX IV. A measurement of such a fill pattern at R1 using the SPAD detector is presented in Figure 4.3. Compared to Figure 4.1, there are a few differences. The first is the bunch length. Bunches in Figure 4.3 have FWHM of about 835 ps, in contrast to the near-natural bunch lengths of around 120 ps presented in the low-current case discussed in section 4.1. This elongation is expected, as discussed in section 2.5, and indicates how significant the impact of Landau cavities can be on the bunches. Another large difference is the bunch profiles. In Figure 4.3, the effects of Landau cavities is clearly seen, with bunches having two distinct peaks in terms of amount of charge, with a separation in time of $\Delta t_{pp} = 600\,\text{ps}$. As discussed in section 2.5, the effect of Landau cavities is barely noticeable when operating the beam at low-current, but at high currents, the emergence of double-peaked bunches becomes evident. In terms of bunch length, the deconvolution barely makes a difference, as deconvolved bunches are on average less than a picosecond shorter than the raw bunches. Nevertheless, deconvolution is important for the bunch profile itself, as it can remove artefacts from the TTS, such as the additional peak at 1.2 ns after the main peak which appears when using the PMA detector, as seen in 4.2.

In the high-current case, where the bunches no longer follow a Gaussian profile, the difference in resolution of the PicoHarp at the different rings becomes evident. As discussed in section 3.6, resolution is worse
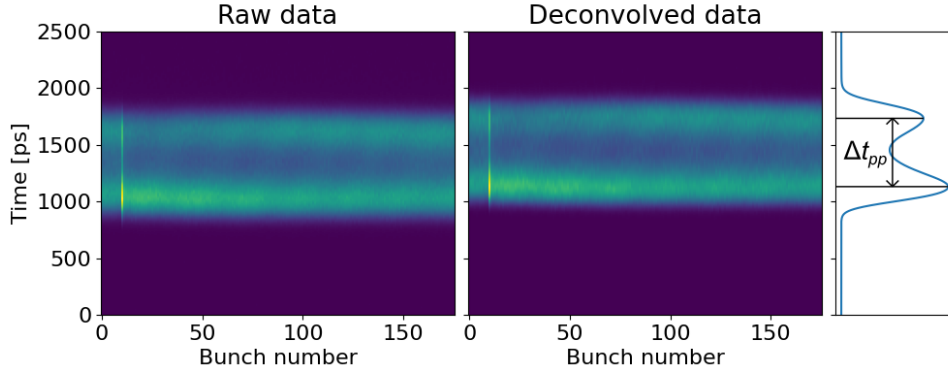
Figure 4.3: Measurements of a high-current (approx. 400 mA) near-homogeneous fill pattern using the SPAD detector at R3. The average peak-to-peak separation in time Δt_{pp} is 600 ps. Note that bunch number 10 contains significantly more charge than other bunches. The profile on the right-hand side is the average bunch profile after deconvolution. The vertical axis is the same for the three plots.

by a factor of 4 at R3 compared to R1. This difference becomes clear when attempting to investigate intra-bunch structure. Figure 4.4 highlights the resolution concerns at R3 compared to R1, by presenting two high-current bunch profiles side-by-side. The important difference to highlight in this comparison is the region between the two main peaks of each bunch. Note that the data before deconvolution has been interpolated in both cases. In the profile measured at R3 (on the right), there is a small peak (or bump) between the two main peaks of the profile. There is little reason to expect such a bump from theory in the case of a homogeneous fill pattern, and likely its emergence arises randomly in combination with the relatively poor resolution of 32 ps/bin at R3. The peak carries over into the profile after interpolating, and remains even after deconvolution. The profiles from R1 do not suffer from the same problem. It is possible that artefacts of this kind can be largely accounted for by smoothing data, at the cost of some amount of information. Nevertheless, the resolution issue at R3 remains, and poses a limitation of the TCSPC setup as it stands. Another possibility to resolve this issue would be to set the resolution of the PicoHarp to 8 ps/bin, but as this would mean that only a bit more than a quarter of a revolution could be covered in a histogram, this option defeats the purpose of trying to measure all bunch profiles in the ring simultaneously.

4.3 Bunch profiles in a <u>high-current inhomogeneous</u> fill pattern

This section is dedicated to the study of an inhomogeneous fill pattern of a high-current beam. Figure 4.5 shows such a fill pattern before and after deconvolution, measured at R1 using the SPAD detector. It has three gaps, each corresponding to two buckets in width. A number of features are apparent. One feature, which contrasts fill patterns considered so far in this chapter, is that bunches no longer appear close to symmetric. As discussed in section 2.5, this is due to gaps in the fill pattern causing differences in the
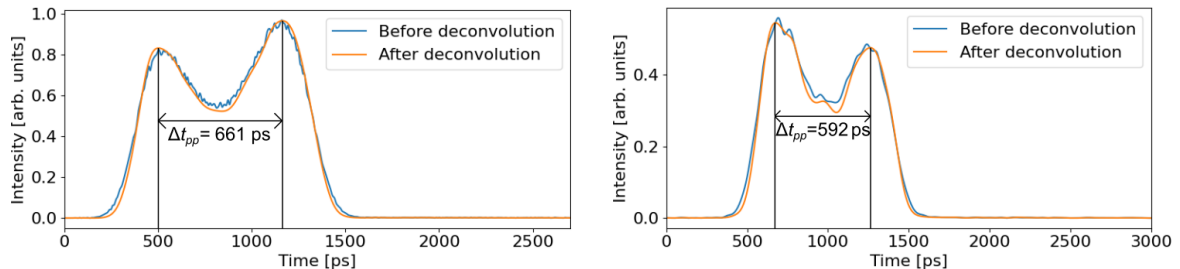

Figure 4.4: Examples of bunch profiles in a near-homogeneous fill pattern measured at high current (each at about 400 mA) at the respective rings, both using the SPAD detector. Left: R1. Right: R3. The peak-to-peak separation Δt_{pp} is shown in each case. The deconvolved profiles have been shifted to overlap with the interpolated profiles for clarity.
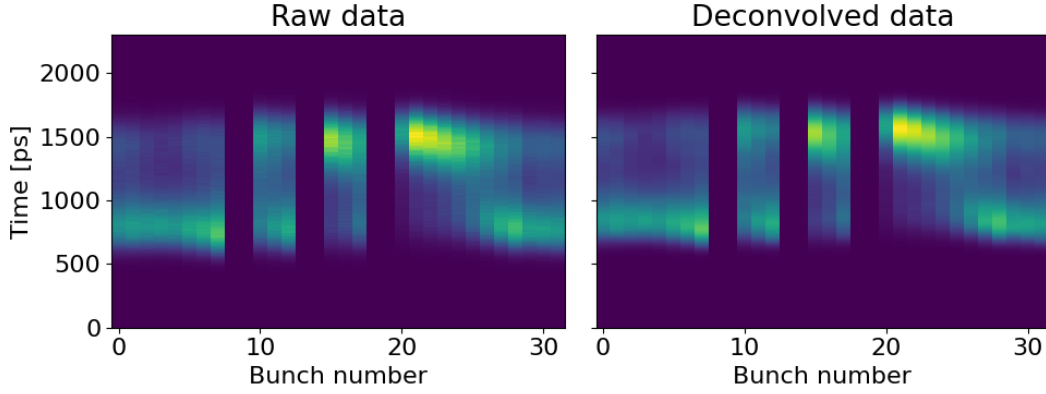
Figure 4.5: An inhomogeneous fill pattern measured at R1 using the SPAD detector at a current of about 350 mA. There are three gaps, each two buckets wide, pairwise separated by 3, 3, 20 non-empty buckets. Left: raw (interpolated) bunch profiles. Right: deconvolved bunch profiles.

voltages experienced by bunches in the Landau cavities. With the introduction of gaps, the potential experienced by bunches is no longer symmetric, leading to asymmetric bunches (consider, for reference, if the potential presented in Figure 2.3 was asymmetric about the synchronous phase). Another feature, also pertaining to bunch asymmetry, is the gradual shift of bunch peak positions. Visualizing this effect is best done by considering the region starting at bunch number 20 in a plot in Figure 4.5, and following the horizontal axis in order of increasing bunch number. The peak position of the first five or so bunches is around 1500 ps, with a gradual transition to a double-peak structure, until peak positions settle at around 800 ps, which carries on around the revolution until the gap is reached. The constancy of bunch peak position in this region reflects the relative homogeneity of the fill pattern there. The same general shift can even be observed in the two regions of three buckets between the gaps. A complete quantitative characterization of the transient in terms of bunch lengths and bunch peak positions is outside the scope of this work. Nevertheless, Figure 4.5 shows that the current implementation of TCSPC at the storage rings of MAX IV laboratory has the capacity to investigate such phenomena in greater detail.

Figure 4.6 shows the deconvolved bunch profiles presented in Figure 4.5 overlayed in the same plot. In this figure, it can be seen that bunch profiles vary significantly across the fill pattern. The features that were discussed with respect to Figure 4.5 are visible, namely that peak positions do generally not overlap and that bunches do not appear symmetric. In particular, some bunches appear single-peaked, the peak located close to either bunch edge, but with a plateau in the other direction. A feature worth pointing out is that all bunches have approximately the same length in terms of start and end points, of about 1250 ps.
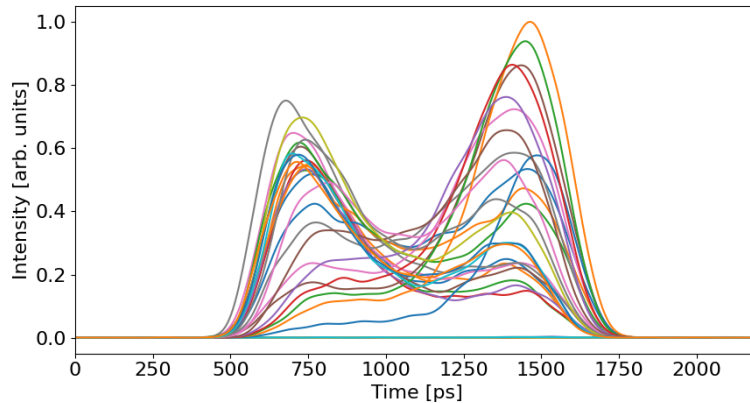

Figure 4.6: Deconvolved bunch profiles presented in Figure 4.5 overlayed. Note that the time scale on the horizontal axis is slightly shorter than the vertical axis in Figure 4.5.

4.4 Comparison of PicoHarp and streak camera data

To begin a more direct and in-depth comparison between streak camera data and PicoHarp data, consider Figure 4.7, where measurements of a fill pattern carried out in parallel at R3 using the streak camera on the left and the PicoHarp and SPAD detector on the right are presented.
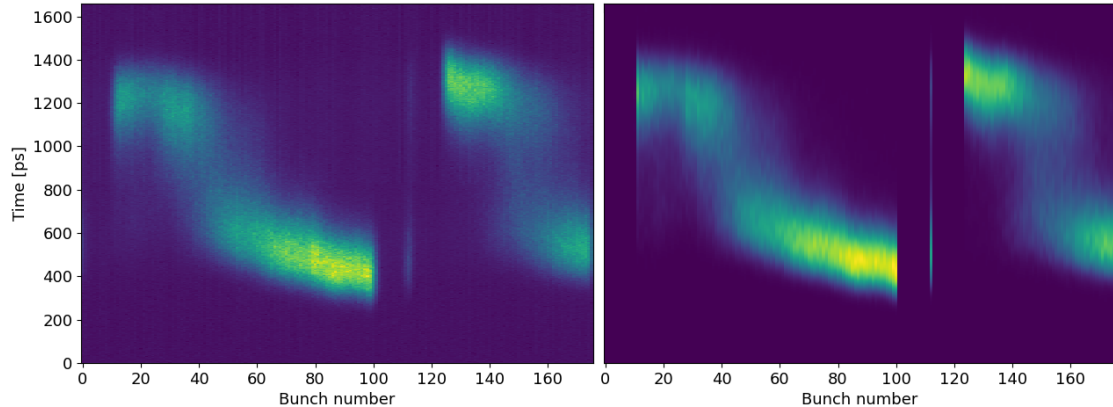

Figure 4.7: An inhomogeneous, high-current (about 400 mA) fill pattern at R3 measured using the streak camera and the PicoHarp with the SPAD detector. The PicoHarp data has been interpolated and deconvolved. Left: Streak camera data. Right: PicoHarp data. The vertical axis is the same for the two plots.

Comparing the plots, they are in good agreement. Maxima in terms of charge are in similar positions, and the bunch lengths are similar. One immediate observation is the noise level is significantly lower in the PicoHarp-plot on the right. This is owing to the long integration times of the PicoHarp and low dark count rate of the detectors. In combination with a sufficient integration time, the signal-to-noise ratio of a typical TCSPC measurement is about $10^{2.5}$. Another distinguishing feature between the two plots is that in the streak camera plot, bunches overlap horizontally. This effect is most clearly visible when considering the single bunch at bunch number 112. In the PicoHarp-plot on the right, it is clearly visible that it occupies only a single bucket, while the streak camera data is slightly blurred, making it seem as though the adjacent buckets are non-empty. This is a significant advantage the PicoHarp provides over the streak camera when measuring bunch profiles; the fact that bunch profiles of adjacent bunches do not overlap. To make a more quantitative comparison between the two measurement methods, the root-mean-square (RMS) bunch lengths σ_z calculated from each data set can be compared. Figure 4.8 presents the RMS bunch lengths of bunches presented in Figure 4.7. The blue line corresponds to PicoHarp data, while the orange line corresponds to streak camera data. It should be noted that the bunch profiles taken from the streak camera data used to calculate the bunch lengths σ_z have been smoothed using a moving average.
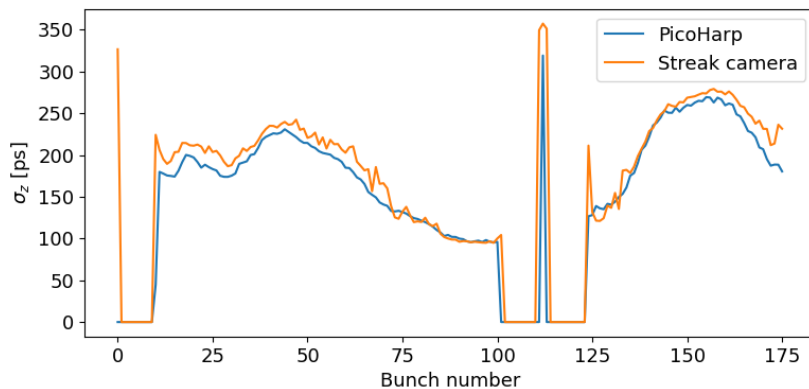

Figure 4.8: RMS bunch lengths σ_z for each bunch presented in Figure 4.7. Note that the streak camera data used to calculate the bunch lengths has been smoothed using a moving average.
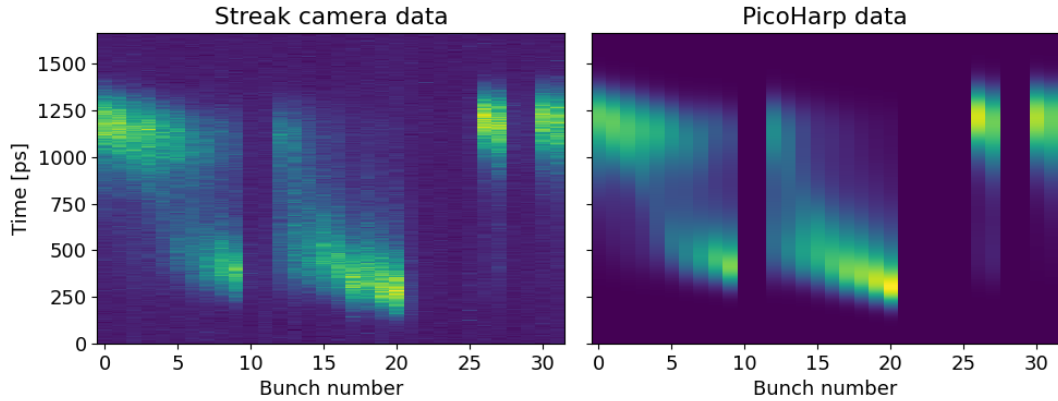
Figure 4.9: An inhomogeneous, high-current (400 mA) fill pattern at R1 measured using the streak camera and the PicoHarp with the PMA detector. The PicoHarp data has been interpolated and deconvolved. Left: Streak camera data. Right: PicoHarp data.

Overall, the calculated bunch lengths are in good agreement. There are a few notable differences, however. The most striking is the long bunch at index 1 calculated from streak camera data. This is another example of a fictitious bunch. It stems from overlap of bunches on the opposite end of one revolution, as the streak camera integrates counts over many revolutions. This same phenomenon of bunch overlap is visible in bunches number 101 and the two bunches surrounding the single bunch at index 112. Another noteworthy feature of Figure 4.8 is that tendentially, the streak camera measures longer bunches than the PicoHarp. Likely, this is because of the worse signal-to-noise ratio of data produced by the streak camera compared to the PicoHarp, resulting in bunch edges appearing less sharp in streak camera measurements.

For completeness' sake, Figure 4.9 shows an inhomogeneous fill pattern measured at R1 using both the streak camera and the PicoHarp with the PMA detector. Again, the plots in Figure 4.9 are in good agreement. The same issues of bunch overlap and noise which were brought up earlier still apply, and the conclusion that the PicoHarp has an advantage over the streak camera in these regards still stands. The RMS bunch lengths measured using the two different methods are presented in Figure 4.10.
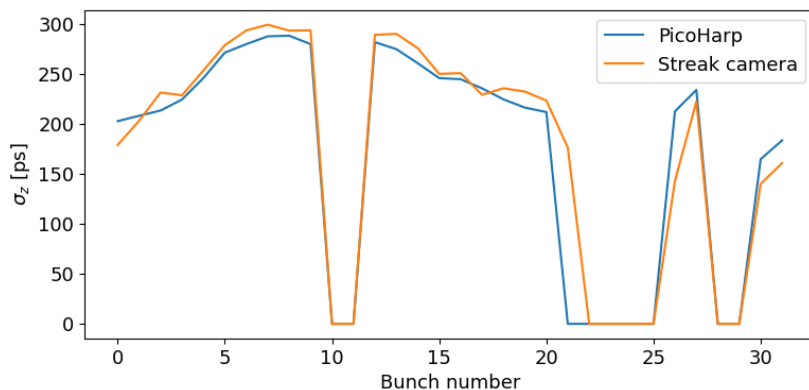

Figure 4.10: RMS bunch lengths σ_z for each bunch presented in Figure 4.9. Note that the streak camera data used to calculate the bunch lengths has been smoothed using a moving average.

The trend is the same as in Figure 4.8, that the streak camera generally measures longer bunches than the PicoHarp, although it can be argued that the trend is not as strong. The issue of bunch overlap creates another fictitious bunch, at index 22. There is one large disparity between the streak camera and PicoHarp measurements, however, namely at bunch number 26, where the PicoHarp measures a significantly longer bunch.

5 Outlook

The aim of this thesis was to act as a first proof of principle with regard to the implementation of TC-SPC as a method of measuring longitudinal bunch profiles at MAX IV. Overall, the goal was achieved, as TCSPC measurements can indeed be used to determine various types of bunch profiles, as discussed in chapter 4. Furthermore, the current implementation of TCSPC is able to measure all bunch profiles in a ring simultaneously and individually, as was the ambition. As seen in section 4.4, light from different bunches do not overlap in TCSPC measurements, and all bunch profiles in a fill pattern can be measured simultaneously. This, in combination with the high signal-to-noise ratio, is a significant improvement compared to previous measurement systems, particularly the streak camera. It should also be pointed out that data from TCSPC measurements is in good agreement with data from streak camera measurements. As the latter are treated as a reference, the resemblance speaks in favor of the TCSPC measurements. In addition, the robustness of the TCSPC system makes it a suitable candidate to continuously and reliably monitor bunch profiles during operation.

In this work, the focus was on determining the total system TTS of each measurement system (differentiated by the combination of detector and ring), and to account for it by using it to deconvolve raw histogram bunches. The implementation of a deconvolution scheme was rather successful, as shown in chapter 4, where the deconvolution was applied to measurements of different fill patterns, and the corrected bunch profiles were in good agreement with the streak camera measurements. The process of determining the total system TTSs is also where the main limitation of this work lies. It was assumed that bunch profiles should not affect the system TTS, the argument for this being that the detectors used are single-photon detectors, and should thus not differentiate between different photons. However, as shown in Figure 3.5, this assumption may not be entirely correct, as a TTS obtained for a given system differs depending on the natural bunch length of the used low-current bunches, though there is a degree of uncertainty with regard to the natural bunch lengths measured with the streak camera. A more detailed investigation of whether bunch profiles do in fact affect the determined system TTSs, when finding the latter using low-current bunches, is something that could be investigated in a further development of TCSPC as a measurement tool at MAX IV. Another approach that could be taken to determine the total system TTSs is to attempt to determine the contributions from each individual component, and convolve them. It should be noted, however, that this approach also requires investigating whether the individual detector TTSs depend on bunch profiles.

Another limitation of the current TCSPC setup, which is understood but still worth mentioning is the relatively worse resolution of the measurement setup at the larger storage ring (R3) compared to the smaller ring (R1), owing to the wish of covering one entire revolution in time in a PicoHarp histogram. An effect of the lack of resolution was highlighted in section 4.2, where a small peak appeared between the two main peaks of a double-peaked bunch. It is possible to increase the resolution of a histogram by covering less than one entire revolution, which may be a possibility when studying a homogeneous fill pattern, as bunches are close to identical. Nevertheless, it can be argued that this defeats the purpose of measuring all bunch profiles simultaneously. Thus, as it stands, measurements of longitudinal intra-bunch structure are more limited at R3 than at R1 if all bunches in each ring are to be studied simultaneously.

Another step that could be taken to improve TCSPC measurements is to implement a correction for the dead time of the PicoHarp. Corrections of this kind to TCSPC measurements have been carried out at other synchrotron light sources, such as [1]. This issue was only very briefly mentioned in section 2.6, but can lead to an underestimation of charge in bunches following a gap [9]. It should be noted that this dead-time effect is minor in case of a homogeneous fill pattern, but if TCSPC measurements are to be used to study inhomogeneous fill patterns, this effect will need to be accounted for. It is possible to remedy the dead-time effect significantly in the current setup, by decreasing the count rate of the detector using ND filters, but a corresponding correction of data remains a possible next step towards a more complete data treatment.

Despite these limitations, it should be emphasized that the implementation of TCSPC presented in this work as a tool to measure longitudinal bunch profiles is a significant improvement over conventional measurement methods, such as using an optical sampling oscilloscope or a streak camera. The bunch profiles of all bunches can be measured simultaneously without light from adjacent bunches interfering.

In combination with the signal-to-noise ratio of a typical TCSPC measurement of about $10^{2.5}$, this allows for a more precise determination of bunch profiles than before. Moreover, owing to the several reiterations and improvements of the measurement setup throughout this work, and the fact that the deconvolution algorithm has been implemented successfully, all the pieces are in place to begin using the developed TCSPC setup as a standard diagnostic tool at MAX IV laboratory.

References

[1] B. Kehrer et al., in *Proc. 9th International Particle Accelerator Conference (IPAC'18), Vancouver, BC, Canada, April 29-May 4, 2018* (JACoW Publishing, Geneva, Switzerland, 2018), Number 9 in International Particle Accelerator Conference, pp. 2219–2222, **DOI** `doi:10.18429/JACoW-IPAC2018-WEPAL027`

[2] B. Xu et al., in *Proc. of International Beam Instrumentation Conference (IBIC'17), Grand Rapids, MI, USA, 20-24 August 2017* (JACoW, Geneva, Switzerland, 2018), Number 6 in International Beam Instrumentation Conference, pp. 168–171, **DOI** `https://doi.org/10.18429/JACoW-IBIC2017-TUPCC09`

[3] K. Wille, *The Physics of Particle Accelerators: An Introduction*, The Physics of Particle Accelerators: An Introduction (Oxford University Press, 2000), ISBN 9780198505495

[4] M. Sands, *The Physics of Electron Storage Rings: An Introduction*, Vol. 6906161 (1969)

[5] H. Wiedemann, *Particle Accelerator Physics*, SpringerLink: Springer e-Books (Springer Berlin Heidelberg, 2015), ISBN 9783319183169

[6] P. Schreiber, Ph.D. thesis, Karlsruher Institut für Technologie (KIT) (2022), DOI: 10.5445/IR/1000148354

[7] A. Rosborg, Doctoral thesis (compilation), MAX IV Laboratory (2012)

[8] T. He et al., Phys. Rev. Accel. Beams **25**, 024401 (2022), **DOI** `10.1103/PhysRevAccelBeams.25.024401`

[9] M. Patting et al., in *Photon Counting Applications, Quantum Optics, and Quantum Cryptography*, edited by M. Dusek et al., International Society for Optics and Photonics (SPIE, 2007), Vol. 6583, p. 658307, **DOI** `10.1117/12.722804`

[10] J. Breunlin, Å. Andersson, in *Proc. of International Particle Accelerator Conference (IPAC'16), Busan, Korea, May 8-13, 2016* (JACoW, Geneva, Switzerland, 2016), Number 7 in International Particle Accelerator Conference, pp. 2908–2910, **DOI** `doi:10.18429/JACoW-IPAC2016-WEPOW034`

[11] W.H. Richardson, J. Opt. Soc. Am. **62**(1), 55 (1972), **DOI** `10.1364/JOSA.62.000055`